12-20-2020

Bacteria-mediated synthesis of cobalt(II,III) oxide nanostructures

Ryan Loughran
Bridgewater State University

Bacteria-mediated synthesis of cobalt(II,III) oxide nanostructures

Ryan Loughran

Submitted in Partial Completion of the
Requirements for Departmental Honors in Chemical Sciences

Bridgewater State University

December 20, 2020

Dr. Saritha Nellutla, *Thesis Advisor*

Dr. Cielito DeRamos King, *Committee Member*

Dr. Alyssa R. Deline, *Committee Member*

Acknowledgements

Special thanks go to Dr. Saritha Nellutla for her superb mentorship throughout the entirety of this project. I would also like to thank Dr. Alyssa Deline and Dr. Tammy King for their feedback and service on my Thesis reading committee.

At Northeastern University, I would like to thank Mr. Bill Fowle for assistance with scanning electron microscopy and energy-dispersive x-ray spectroscopy analysis of samples. At the University of Rhode Island, I would like to thank Dr. Irene Andreu for the same.

Dr. Mark Turnbull from Clark University assisted with gathering data using electron paramagnetic resonance spectroscopy and super-conducting quantum interface device magnetometry, and so I would like to thank him for his time and for allowing us to use his instrumentation.

Dr. Peter Setlow at the University of Connecticut and Dr. Eric Brown at McMaster University were also integral in helping explain the physiology of bacteria and offering insight into mutations and teichoic acids. Without them, I certainly would have lacked the bacterial knowledge necessary to form any hypotheses involving mechanisms of product formation.

At Bridgewater State University, I would like to thank Ms. Jessica Campbell for offering much of her time to teach me how powder x-ray diffraction works and to run samples for us. I would like to thank the Department of Biological Sciences for fruitful discussions and specifically Dr. Jenna Mendell for training me on bacterial culturing and sterile techniques.

I would also like to thank the entire Department of Chemical Sciences, as I met with every faculty member at some point and received advice, insight, permission to borrow chemicals or instrumentation, or a combination of all of these.

This project also would not have been possible without funding. The Adrian Tinsley Program generously provided funding through several Semester Research Grants as well as the Summer Research Grant. Additional funding came from the Dr. Vahe Marganian Research Scholarship awarded to me in 2019, and CARS small grants awarded to Dr. Saritha Nellutla.

The Adrian Tinsley Program also provided the opportunity to present my research locally at Bridgewater State University and Clark University, as well as nationally at the American Chemical Society's National Meeting in Orlando, FL in 2018. These opportunities allowed me to receive feedback from industry and research professionals who otherwise would be outside my sphere of influence.

To all who contributed to making this project possible, I sincerely thank you.

Table of Contents

List of Figures and Tables

Content **Page Number**

Abstract

Metal oxide nanomaterials have a wide-range of applications that are often related to their structure-property relationships. Cobalt(II,III) oxide (Co_3O_4) is of particular interest due to its potential use in superconductors, gas detection and battery efficiency, among other applications. This work describes the synthesis of Co_3O_4 using rod-shaped Gram-positive bacteria *Lactobacillus rhamnosus* as a template. The motivation behind this project was to find potentially cheaper and environmentally benign protocols in comparison to the current solution-based methods. The effect of various synthesis conditions have been explored on the morphology of Co_3O_4 using scanning electron microscopy and a mechanism behind the formation of Co_3O_4 rods has been proposed. Understanding the surface chemistry of the bacteria and how it interacts with the metal cation can potentially lead to a generalized synthesis procedure that is easily applicable to other metal oxide and Gram-positive bacteria combinations with tunable morphologies.

1. Introduction

1.1. Metal oxide nanomaterials and their applications

Metal oxides, specifically at the nanoscale (i.e. with dimensions at or below 100 nm), are being used and investigated for a wide array of potential applications[1–7]. Metal oxides feature one or more metal cations coordinated by oxide ions, and include such species as Al_2O_3, MgO, Fe_3O_4 and SnO, among many others. For example: metal oxides with conducting properties are suited for applications in electrochemistry[8,9]; metal oxides with high porosity crystal structures are well-suited for gas capture[10]; photoactive metal oxides are used in photocatalytic applications[11]; magnetic metal oxides are being explored for quantum computing, hyperthermia or targeted drug delivery[2,12].

There are numerous methods established to produce nanomaterials on a lab-scale, and a few metal oxide nanomaterials can already be obtained on a much larger production-scale[13]. However, common solution-based methods primarily produce spherical nanoparticles. Synthesis of other morphologies via solution-based methods require complex design protocols and/or expensive instruments or rely on natural evolution based on thermodynamics and kinetic principles[7,13,14]. This can be disadvantageous because many properties such as catalytic performance, environmental remediation, energy conversion and quantum computing depend on the morphology of the nanomaterial[1,13,15]. Hence, it is important to be able to synthesize nano-systems with a precise control over size as well as shape. Additionally, since many existing procedures can be limited by high-cost and hazardous reagents and/or by-products[16,17], it is intuitive to develop environmentally-benign and tailored synthetic procedures to produce a nanomaterial with desired shape and size. Hence, scientists have begun looking at using plant extracts, proteins, and bacteria as a scaffolding medium to produce various nanomaterials[6,16,18].

1.2. Cobalt(II,III) oxide

1.2.1. Structure

This project focuses on cobalt(II,III) oxide (Co_3O_4). Co_3O_4 is an example of a class of metal oxides that crystallize in a normal spinel structure ($A^{2+}B^{3+}{}_2O_4$) with close-packing of cations and anions[19,20] (see Fig. 1.1). In Co_3O_4, oxide ions form a face-centered lattice with Co^{2+} occupying one-eighth of the tetrahedral holes and the Co^{3+} occupying one-half of the octahedral holes. As one would expect, Co^{2+} ions are surrounded by four O^{2-} ions and Co^{3+} ions are surrounded by six O^{2-} ions. Each unit cell contains eight formula units, resulting in a composition of $A_8B_{16}O_{32}$.

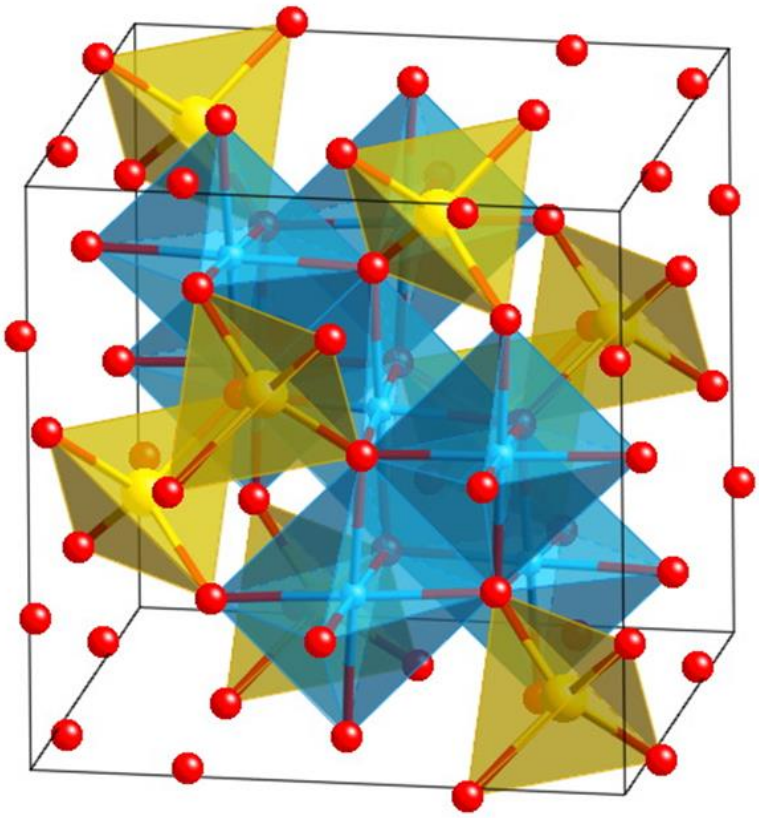

Figure 1.1. The cubic spinel crystal structure of cobalt(II,III) oxide. In the figure, the yellow tetrahedra represent the Co^{2+} coordinated with O^{2-} (red) while the blue octahedra represent the Co^{3+} coordinated with O^{2-}. The image is reproduced from http://som.web.cmu.edu/frames2.html

1.2.2. Applications

Co_3O_4 was chosen because it is being explored for a wide variety of applications, including battery technology, microelectronics, superconductors, temperature and gas sensing, and solar energy absorbers[10,21]. With a growing list of potential applications, it is imperative to have a reliable synthesis procedure that can provide Co_3O_4 inexpensively and is produced with minimal environmental repercussions.

1.2.3. Limitations

As mentioned earlier, solution-based procedures for synthesis of many metal oxide nanomaterials exist, including for the synthesis of Co_3O_4. Often, these procedures involve the use of surfactants or known-carcinogenic reactants like $Co(NO_3)_2$ [22]. Reportedly, these procedures are also limited in that they are only able to produce nanospheres[8,19,22] and nanocubes[22,23]. Researchers have sought to overcome these challenges by developing new methods for Co_3O_4 production, including the sol-gel method[19,24], microwave irradiation[25], or through the use of proteins[26,27].

1.3. Previous research

1.3.1. Bacterial template for Co_3O_4 synthesis

This project is inspired by the work of Shim et al.[6], who proposed a comparatively safe, environmentally benign, and inexpensive synthesis procedure using common and fast-growing bacteria as a template upon which Co_3O_4 is formed as layer. They successfully demonstrated the formation of Co_3O_4 as a complete shell around the Gram-positive bacteria *Bacillus subtilis*. Since their work primarily focused on the electrochemical applications of Co_3O_4 nanorods, they did not investigate the mechanism behind their formation. However, they hypothesized that the Co_3O_4 forms through electrostatic interaction between Co^{2+} and the negatively charged teichoic acids of the bacterial surface. Shim et al.[6] did not explain their reasoning in selecting *B. subtilis* as a template, but based on their findings, this project sought to reproduce their experiments and attempt to answer the unanswered questions about the mechanism of Co_3O_4 formation.

1.3.2. *Lactobacillus rhamnosus* as a template

This project began by replicating the synthesis conditions set forth by Shim et al.[6], but it was quickly discovered that *Bacillus subtilis* was not an ideal template because they form endospores when placed in unfavorable environments[28,29], and in doing so their overall surface morphology changes. It is unknown how Shim et al.[6] overcame this, but for the purposes of this project, *Lactobacillus rhamnosus*, a relative of *B. subtilis* was selected. *L. rhamnosus* is also Gram-positive (see Fig. 1.2) and features similar morphology to *B. subtilis*, but the *Lactobacillus* species are incapable of forming endospores[30]. They are rod-shaped, typically with diameters ranging from 0.25 – 1.0 μm and lengths of 4 – 10 μm[31]. As a Gram-positive species, *L. rhamnosus* has an exposed peptidoglycan with phosphate-rich teichoic acids (see Fig. 1.3).

1.4. Project goals

The overarching goal of this project is to *develop reliable and reproducible synthesis protocols using bacteria-templates* that will allow scientists to "custom-design" nanomaterials for their desired applications. Therefore, it is important to identify the "minimum qualifications" for the Gram-positive bacterial templates as well as understand the mechanism behind the formation of nanomaterials on these templates.

The specific goals of this project are therefore as follows:

1. To establish synthesis conditions, using *L. rhamnosus* bacteria, for producing high purity Co_3O_4 nanomaterial consistent in size and shape, and
2. To understand the mechanism of Co_3O_4 formation by evaluating the effect of synthesis conditions on the morphology and purity of Co_3O_4 produced. Specifically,
   a. the role of teichoic acids in coordinating Co^{2+} ions, and
   b. the importance of the magnitude of negative bacterial surface charge.

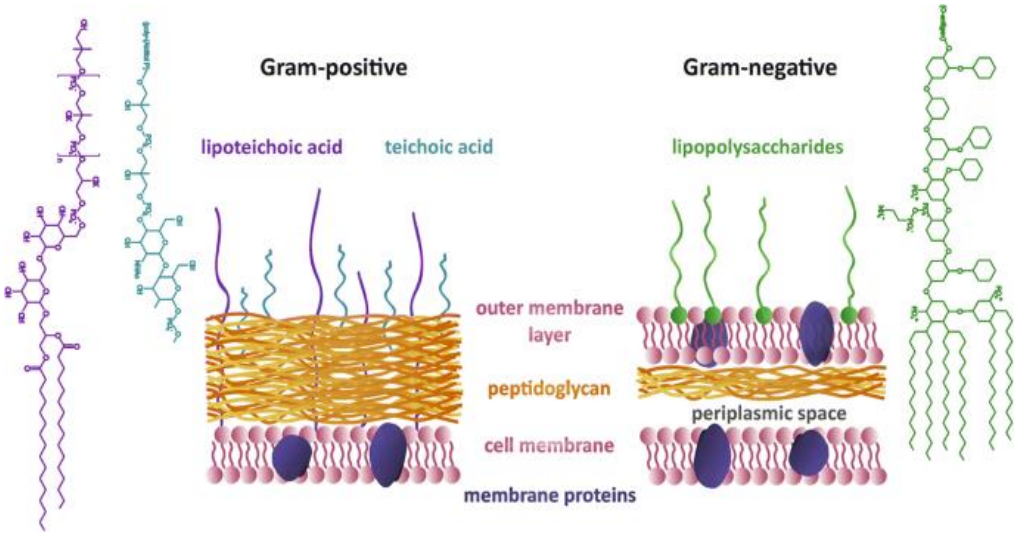

Figure 1.2. A cartoon representation of cell wall structure in Gram-positive vs. Gram-negative bacteria. The surface of a Gram-positive bacterial species, like *L. rhamnosus*, is rich in teichoic acids stemming from the exposed peptidoglycan. Teichoic acids feature a number of repeating phosphate groups, giving them a highly negative charge. Conversely, a Gram-negative species has lipopolysaccharides embedded in a cell membrane, which is largely non-polar. Image is reproduced from *J. Nanoparticle Res*. **2019**, 21 (8).

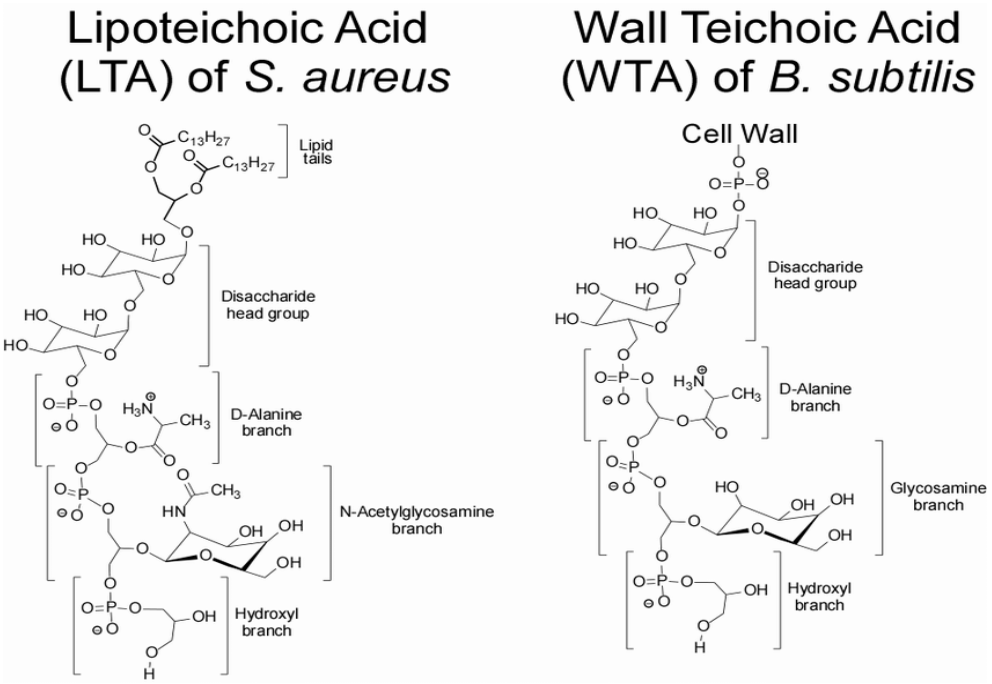

Figure 1.3. Chemical structure of lipoteichoic acids and wall teichoic acids. The structural differences between these can include sugar constituents and number of repeating units, both of which could affect the hypothesized mechanism of formation. Image reproduced from *Instruments, Methods, Mission. Astrobiol. XI* ***2008****,* 7097 (March), 70970O.

2. Experimental Details

2.1. Materials

Freeze-dried chloramphenicol-resistant *Lactobacillus rhamnosus* was obtained from the American Type Culture Center (ATCC, 27773). MRS Broth (Difco) and chloramphenicol (99%, Alfa Aesar) were obtained from Fisher Scientific. ACS reagent-grade (purity of ≥ 95%) cobalt(II) chloride hexahydrate and sodium borohydride, as well as glycerol were purchased from Fisher Scientific. Additionally, Tween-80, 2-propanol, sodium citrate trihydrate, polyvinylpyrrolidone (PVP) and polyethylene glycol (PEG) were also purchased at ACS-grade level from Fisher Scientific. Each chemical was used as received without further purification.

2.2. Synthesis and characterization methods

2.2.1. Bacterial preparation

MRS broth preparation: MRS broth was prepared according to the instructions provided by the distributor i.e., mixing MRS broth powder in boiling water at a ratio of 55 g powder per 1 L DI water. After stirring for 2 minutes, the broth was transferred to an autoclavable Pyrex bottle and autoclaved at 120 °C with a 20-minute exposure time. After cooling to room temperature, chloramphenicol was added at a ratio of 0.02 mg chloramphenicol per 1 mL broth and was gently shaken to dissolve the antibiotic. The broth was then tightly sealed and stored in a refrigerator until further use. If unopened, the broth can be stored up to 30 days in a refrigerator. Once opened, however, it should be used within 7 days, as the antibiotic will not hinder growth of any fungal contaminants that may enter the open bottle.

Growing bacteria culture: Colonies of *L. rhamnosus* were grown from glycerol stocks (see Supplemental Information) in desired volume of MRS broth at 37.0 °C for 24 - 36 hours in a shaking incubator. Bacteria were then isolated at centrifugation speed of 10,000 rpm for 15 minutes, followed by resuspension in DI water. In some instances, they were re-suspended in 0.1 vol. % Tween-80, as described in the Table S1. The targeted optical density (OD), measured at 600 nm, was originally 0.5 based on the work of Shim et al.[6], but to evaluate its effect on the mechanism, the OD was changed between 0.5 – 2.0. Based on trial-and-error experimentation, the ideal optical density of *L. rhamnosus* for the purposes of this project was determined to be 1.4 - 1.6 at 600 nm. A complete list of the synthesis parameters varied in this project can be found in Table S1.

2.2.2. Co_3O_4 synthesis

To the bacterial resuspension, an aqueous solution of 0.100 M $CoCl_2 \cdot 6H_2O$ was typically added at no more than 10 mL/min while the resuspension was stirred at 300 rpm under atmospheric conditions. Typical volumes ranged from 100 - 250 mL based on the procedure established by Shim et al.[6] After the addition, the mixture was allowed to continue stirring at 300 rpm for 24 - 48 hours. Then, a solution of 0.100 M $NaBH_4$ (typical volumes of 50 - 125 mL, half of the volume of $CoCl_2 \cdot 6H_2O$) was added at no more than 10 mL/min to the stirring Co^{2+} - bacteria suspension and was left to react over 24 - 48 hours in air. The $NaBH_4$ functions as a reducing agent and was used by Shim et al.[6] to produce Co_3O_4 from Co^{2+}. Its exact role is explored more in Results and Discussion section. The resulting precipitate (typically varying in colors from green to brown) was collected using Buchner funnel with Whatman #50 filter paper. The filtered powder was rinsed with DI water and 2-propanol three times each to remove any unbound ions or by-products from the bacteria decomposition. Once dry, the powder was collected and calcined in a quartz boat. The molar ratio of Co^{2+} : BH_4^- was altered frequently between syntheses, as was the addition rate of $CoCl_2 \cdot 6H_2O$. A tabulated overview of all altered synthesis conditions can be found in Table S1.

Calcination was carried out in a Lindbergh TF55035A-1 tube furnace. The sample was ramped to 650 °C over 12 hours, then held at 650 °C for another 12 hours before cooling to room temperature. Calcination was carried out in air, and the calcined powder was nearly always black and very fine. Additional calcination temperatures and ramp rates were tested (cf. Table S1), and their effects on the product are detailed in the Results and Discussion section.

The following flowchart summarizes the synthesis procedure determined to be ideal for Co_3O_4 production using *L. rhamnosus*.

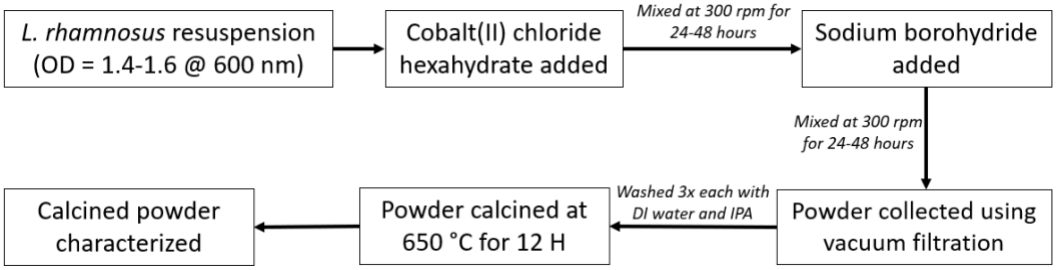

2.2.3. Powder x-ray diffraction (pXRD)

The crystal structure and composition of all the calcined powders were determined using a Rigaku "MiniFlex" Benchtop powder X-Ray Diffractometer. Data was collected from 5 – 90° at 0.01° increments and was used to confirm the crystallinity and phase purity of calcined samples. Peak shape analysis was completed using Origin Pro 2016 software

(Origin Lab Corporation, Northampton, MA, USA) to obtain full width at maximum height (FWHM) values, which in turn were used to determine crystallite size using the Scherrer equation[32]. Details about the peak shape analysis are described in supplementary information.

2.2.4. Fourier-transform infrared (FT-IR) spectroscopy

FT-IR spectra were obtained in the 4000 – 400 cm^{-1} frequency range using a Perkin-Elmer Spectrum Two FT-IR spectrometer. FT-IR was used to determine the presence of Co^{2+} — O and Co^{3+} — O vibrational peaks characteristic of Co_3O_4.

2.2.5. Scanning electron microscopy (SEM) and energy-dispersive x-ray spectroscopy (EDXS)

Initially, surface, morphological and elemental characterization was carried out using a Hitachi S-4800 Field Emission Scanning Electron Microscope (FE-SEM) equipped with an Energy-Dispersive X-Ray unit. Later, morphological characterization was carried out using a Zeiss Sigma VP FE-SEM with an Oxford Instruments X-max 50 mm^2 EDX spectroscope. The powder samples were mounted as a thin layer on a carbon tape and imaged using an accelerating voltage of 3000 V.

2.2.6. Zeta potential

Zeta potential measurements were obtained using a ZetaSizer Nano ZS90. The zeta potentials for each bacterial species was taken in broth, DI water, and cobalt solution. The pH and ionic strengths of each solution were not measured and are therefore not available to help expand upon the data obtained from the zeta potential measurements.

3. Results and Discussion

3.1. Effects of various synthesis conditions on product formation

Table S1 lists the synthesis conditions accompanying all the samples that were made during the course of this project. An abbreviated form of this list is shown in Table 3.1 for samples #5, #7, #8, #11, #15 and #16. These samples were chosen because they represent the successful syntheses that produced morphologies ranging from cubes to octahedra to cylinders. Since these samples are representative of the morphologies observed in this project, correlating their synthesis conditions to the observed morphological differences should provide insights about the mechanism of Co_3O_4 formation on a bacteria template.

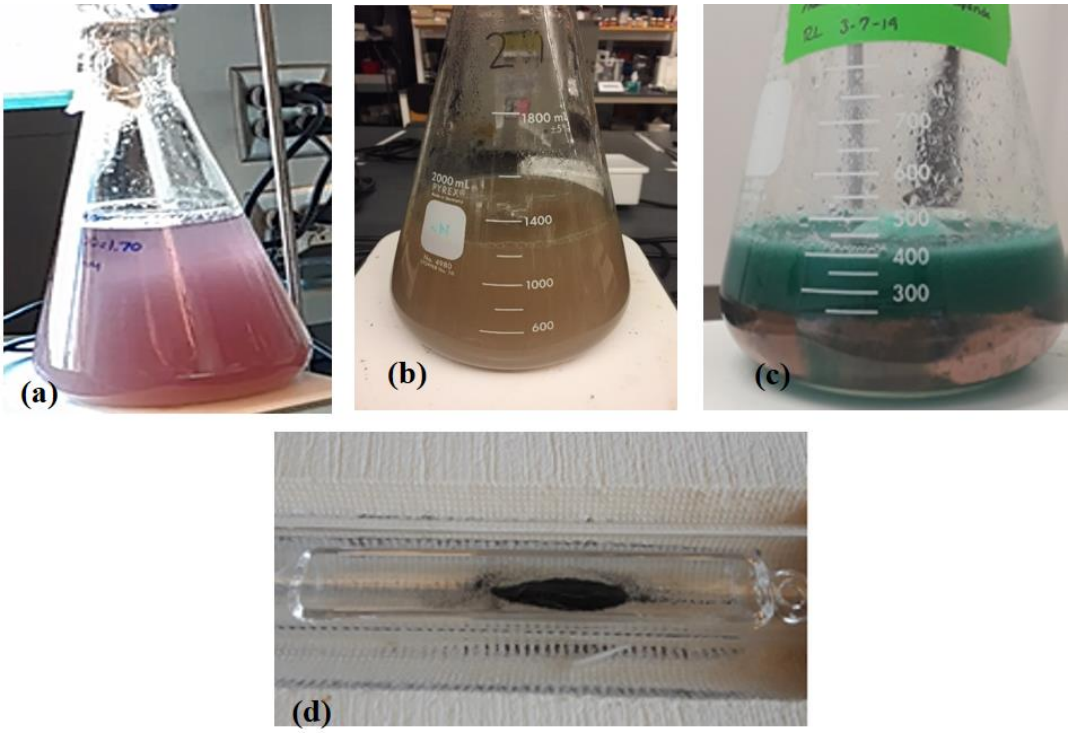

Figure 3.1. (a) The opaque pink color typical of the cobalt-bacterial suspension. (b), (c) Two of the typical colors seen when cobalt, borohydride and bacteria are allowed to mix together for 24 - 48 hrs. (d) Calcined powder of blue precipitate seen in (c). As can be seen the blue coloration of the powder has completely changed to black upon calcination at 650 °C in air.

Prior to calcination, the as-synthesized powders formed from the reaction of $CoCl_2$ with $NaBH_4$ seem to vary. Upon introduction of borohydride to the pink cobalt-bacteria suspension (see Fig. 3.1.a) would often change into various colors (see Figs. 3.1.b and 3.1.c). Further, identical reaction conditions done simultaneously would sometimes produce solutions of different colors. However, calcination of the resulting precipitate very consistently produced a black powder (see Fig. 3.1.d).

Table 3.1. Synthesis conditions of samples #5, #7, #8, #11, #15 and #16. Detailed information about these samples along with all other syntheses carried out in this project can be found in Table S1.

Sample Number	*L. rhamnosus* Optical Density (@ 600 nm)	Resuspended in	Co2+ moles /BH4- moles	Other Compound and its amount	Cobalt Addition Rate	Time with Co^{2+}	Reducing Agent Addition Rate	Time with Reducing Agent	Ramp time to 650 °C
5A	0.5	DI water	1.09		Instant	1 hr	10 mL/min	20 hr	2 hr
5B	0.1	DI water	1.09		Instant	1 hr	10 mL/min	20 hr	2 hr
5C	0.5	DI water	1.09		Instant	1 hr	10 mL/min	20 hr	2 hr
5D	1.0	DI water	1.09		Instant	1 hr	10 mL/min	20 hr	2 hr
7A	0.5	DI water	1.00		Instant	24 hr	10 mL/min	18 hr	3 hr
7B	0.5	0.1 vol % Tween 80	1.00		Instant	24 hr	10 mL/min	18 hr	3 hr
7C	0.5	DI water	1.00		Instant	24 hr	10 mL/min	18 hr	3 hr
7D	0.5	0.1 vol % Tween 80	1.00		Instant	24 hr	10 mL/min	18 hr	3 hr
8A	1.931	0.1 vol % Tween 80	1.10		5 mL/min	1 hr	5 mL/min	16 hr	3 hr
8B	0.406	0.1 vol % Tween 80	1.00		5 mL/min	1 hr	5 mL/min	16 hr	N/A
11	1.467	0.05 vol % Tween 80	1.10		10 mL/min	None	10 mL/min	24 hr	3 hr
15A	0.5	DI water	1.00		10 mL/min	68 hr	10 mL/min	45 hr	12 hr
15B	0.5	DI water	1.94		10 mL/min	68 hr	10 mL/min	45 hr	12 hr
15C	1.5	DI water	2.00	PVP - 1.75 g	10 mL/min	68 hr	10 mL/min	45 hr	12 hr
15D	1.7	DI water	1.00	L-Alanine - 0.02 moles	10 mL/min	45 hr	10 mL/min	72 hr	12 hr
16A	1.995	DI water	1.00		Instant	48 hr	10 mL/min	48 hr	12hr
16B	1.995	DI water	1.00	PEG - 1.1 g	Instant	48 hr	10 mL/min	48 hr	12 hr

The color of $CoCl_2 \cdot 6H_2O$ solution is always pink at the concentrations described in section 2.2.2. Cobalt(II) oxide is known to have a green color in bulk and develops a gray coloration as the particle size decreases. Other cobalt oxy-hydroxides may appear brown, gray, blue, yellow, etc. As such, the general formula for the as-synthesized powder in this project is taken as $Co_xO_y(OH)_z$, while the calcined powder, which is nearly always black, closely matches the color of Co_3O_4 nanomaterials, which are a dark gray with a hint of blue coloration. Metallic cobalt has as a very dark gray color. It is possible that the variety of colors seen in this synthesis can be attributed to minor changes in pH or temperature, or possibly residual cobalt embedded in the walls of the glassware from previous syntheses.

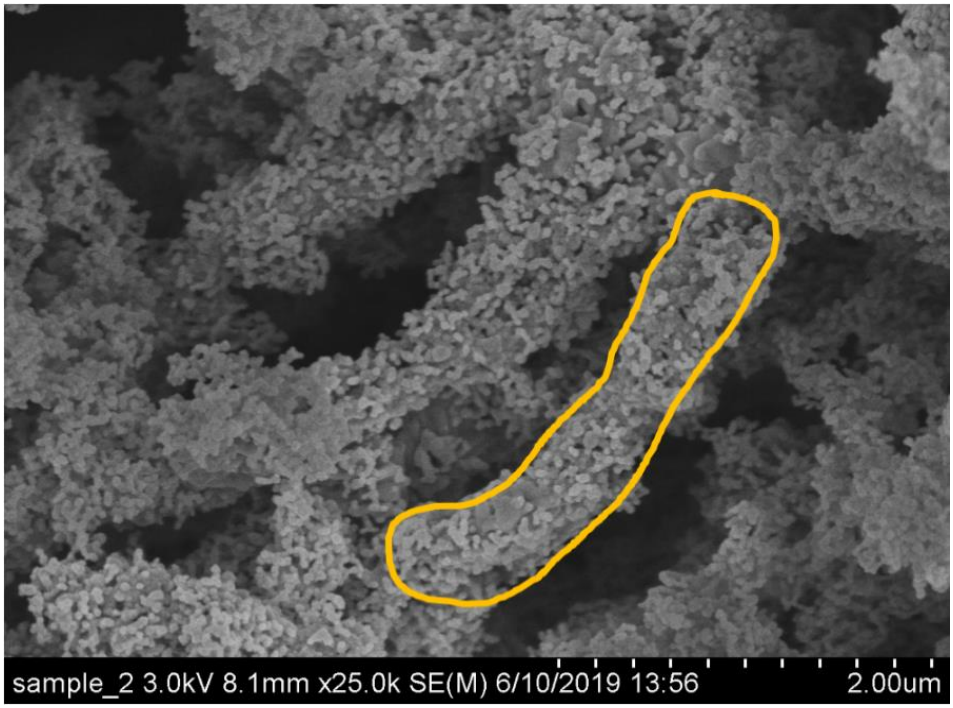

Figure 3.2. A representative SEM image of sample from synthesis #5B. Long ropes (~ 2 - 4 μm long and ~1 μm in diameter) made of small rod-like structures are observed. These dimensions reflect the dimensions of the *L. rhamnosus* used in the synthesis.

SEM analysis (see Fig. 3.2) of sample #5B (OD = 0.1, 1 hr interaction time with Co^{2+}, 20 hr reaction time; cf. Table 3.1) revealed long highly aggregated rope-like structures approximately 2.5 μm in length and 0.5 μm in diameter that somewhat represented the desired product i.e., Co_3O_4 cylinders. Assuming that this is a result of bacterial aggregation, bacteria was re-suspended in 0.1 vol% of Tween-80 (a detergent) instead of DI water and the interaction time between Co^{2+} and the bacteria was increased from 1 hour to anywhere between 12 hr – 68 hr (cf. Table 3.1).

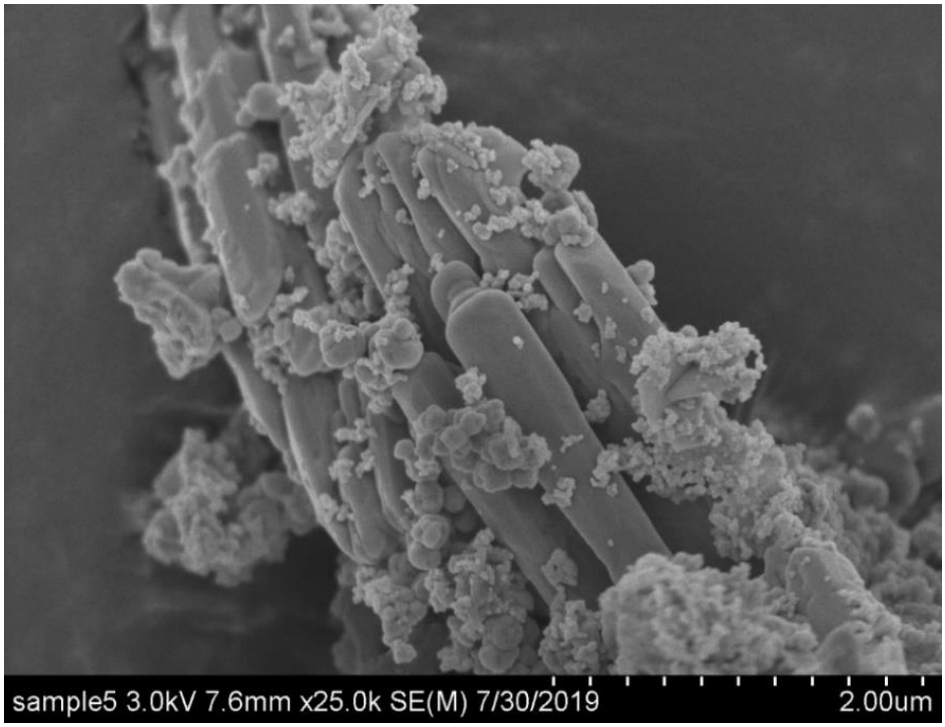

Figure 3.3. The SEM image of sample #7B. The observed clusters closely resemble *L. rhamnosus* and the observed coating was determined to be cobalt oxide from the EDXS analysis. The rods appear to be approximately 2.5 μm long and 0.6 μm in diameter

Figure 3.3 shows an SEM image of sample #7B (OD = 0.5, 24 hr interaction time with Co^{2+}, 18 hr reaction time; cf. Table 3.1). As can be seen from the figure, these changes successfully resulted in 2 - 3 μm-long rods that closely resembled bacteria. Since these rods are aggregated and covered in what EDXS confirmed to be excess cobalt oxides, the ratio of bacteria : Co^{2+} was altered by increasing the optical density of bacteria and decreasing the overall concentration of cobalt added to the bacterial suspension. This was done to theoretically place the bacteria in excess of the cobalt and prevent the excess cobalt from reacting and covering the rod structures. In addition, the calcined samples were subjected to sonication in water bath with or without capping agents such as polyvinyl-pyrrolidone or polyethylene glycol to reduce the aggregation.

While some syntheses (e.g. Sample #8B) failed to yield as-synthesized powders, others (e.g. Sample #13A) produced very fine as-synthesized powders that retained their "fine powder" nature upon calcination at 650 °C (SEM data not shown). Interestingly, some syntheses produced Co_3O_4 with unexpected morphologies. Most notably, sample #11 (cf. Fig. 3.4.a) and sample #16A (cf. Fig. 3.4.b) produced well-defined octahedra of varying sizes. Specific synthesis conditions for these samples can be found in Table 3.1.

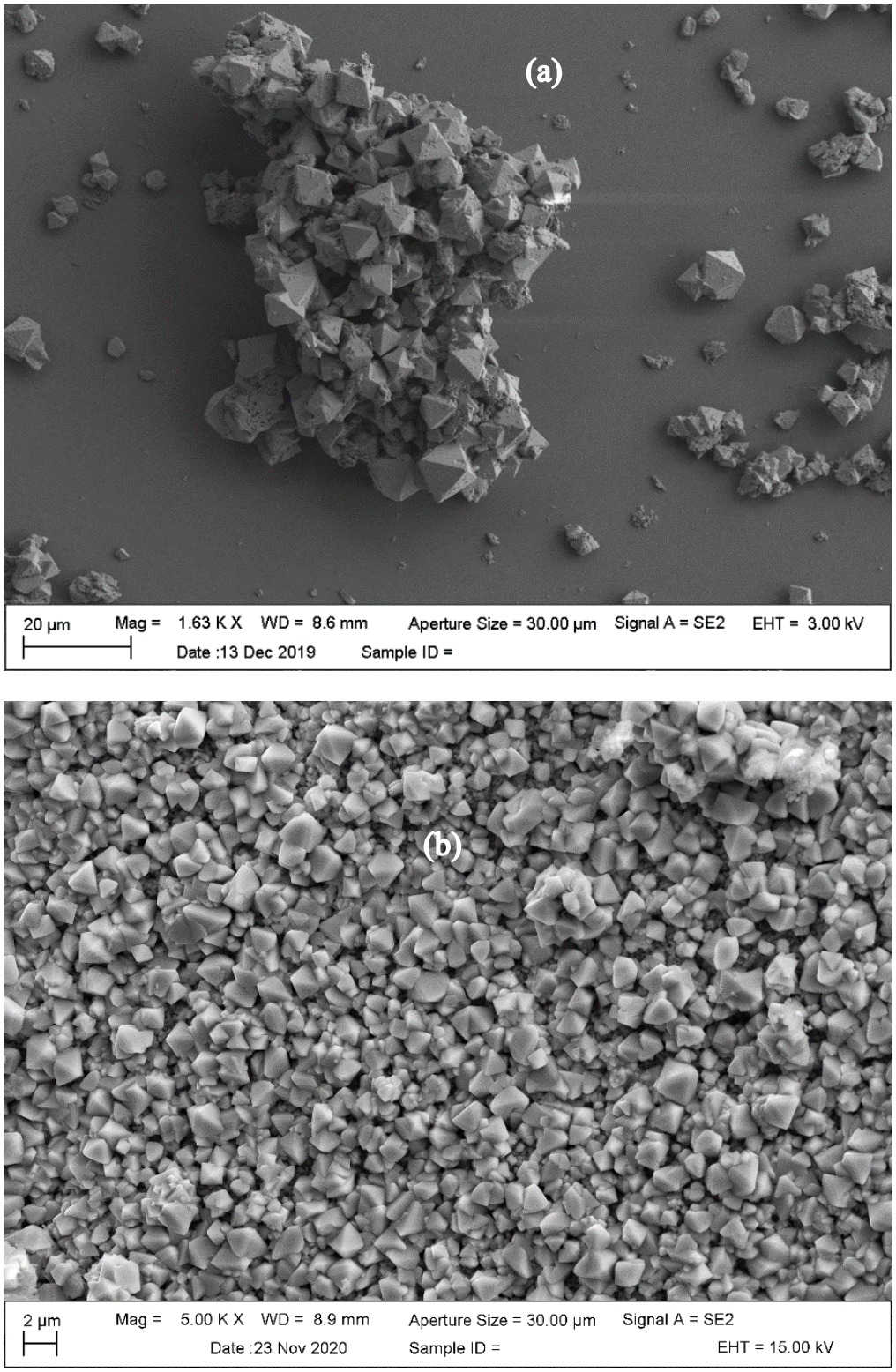

Figure 3.4. Representative SEM images for sample #11 (a) and sample #16A (b). It can be clearly seen that both samples contain octahedra of varying sizes. Synthesis conditions for these samples can be found in Table 3.1 and additional details can be found in the text.

Table 3.2. The peak energy values assigned to cobalt and oxygen in EDXS analysis. These peaks are unique to each element, so the energy associated with them can be attributed to specific elements, in this case cobalt and oxygen.

Cobalt Peaks		**Oxygen Peak**
$K\alpha_1$ @ 6.931 keV	$L\alpha_1$ @ 0.775 keV	Kα1 @ 0.525 keV
$K\beta_1$ @ 7.649 keV	$L\beta_1$ @ 0.790 keV	

Figures 3.5 show the EDX spectra for samples #11 and #16A. The EDX spectroscopy can be used to identify the elements present within a sample while it is examined by FE-SEM. The principle behind EDX spectroscopy is as follows: when core electrons from an atom are dislodged with x-rays, higher-energy electrons replace these 'holes' by releasing the excess energy in the form of x-rays. Since the atomic structure of each element is unique, the observed EDX spectrum is unique to that element as well. Therefore, EDXS allows for the determination of exact elements present within a sample with a high degree of accuracy. Table 3.2 lists the literature peak positions for Co and O[14,33]. It can be clearly seen that Co and O EDXS peaks observed from samples #11 and #16A match very well with the literature values. While the strong peak for Si observed in Fig. 3.5.a is from the Si wafer used for sample mounting, small peaks observed for C and P in Fig. 3.5.b can be attributed to leftover teichoic acids from bacteria. In addition to having no commonality in synthesis parameters (cf. Table 3.1) between these samples, calcined sample #11 was sonicated, while sample #16A was not. Therefore, these unexpected morphologies cannot yet be explained.

Since sonication was introduced into synthesis protocol, no rod-shaped structures were detected in the SEM images. Therefore, in order to elucidate its effect, samples #15 and #16 were prepared without the sonication. In contrast to octahedra seen in sample #16A (cf. Fig. 3.4.b), the calcined sample #15B revealed distinct rods (~1.5 μm long, cf. Fig. 3.6.a) that not only fit the dimensions of *L. rhamnosus* but also much less aggregated than seen in sample #7B (Fig. 3.3). Further, the hollow nature of these rods can be seen in Figure 3.6.b. The EDX spectrum of #15B (Fig. 3.7) is consistent with other samples in the sense that it shows primarily cobalt and oxygen. The large carbon peak can be attributed to the carbon tape used for mounting the sample. Also, a small peak for phosphorous may be attributed to the remains from the bacterial scaffolding. Additionally, as seen from Fig. 3.8., powder XRD spectrum of this sample matches the literature[14] suggesting that rods seen in #15B are most likely Co_3O_4 with cubic spinel. Hence, sample #15B demonstrates that it is quite possible to produce Co_3O_4 rods in the shape of bacteria using *L. rhamnosus* as a template.

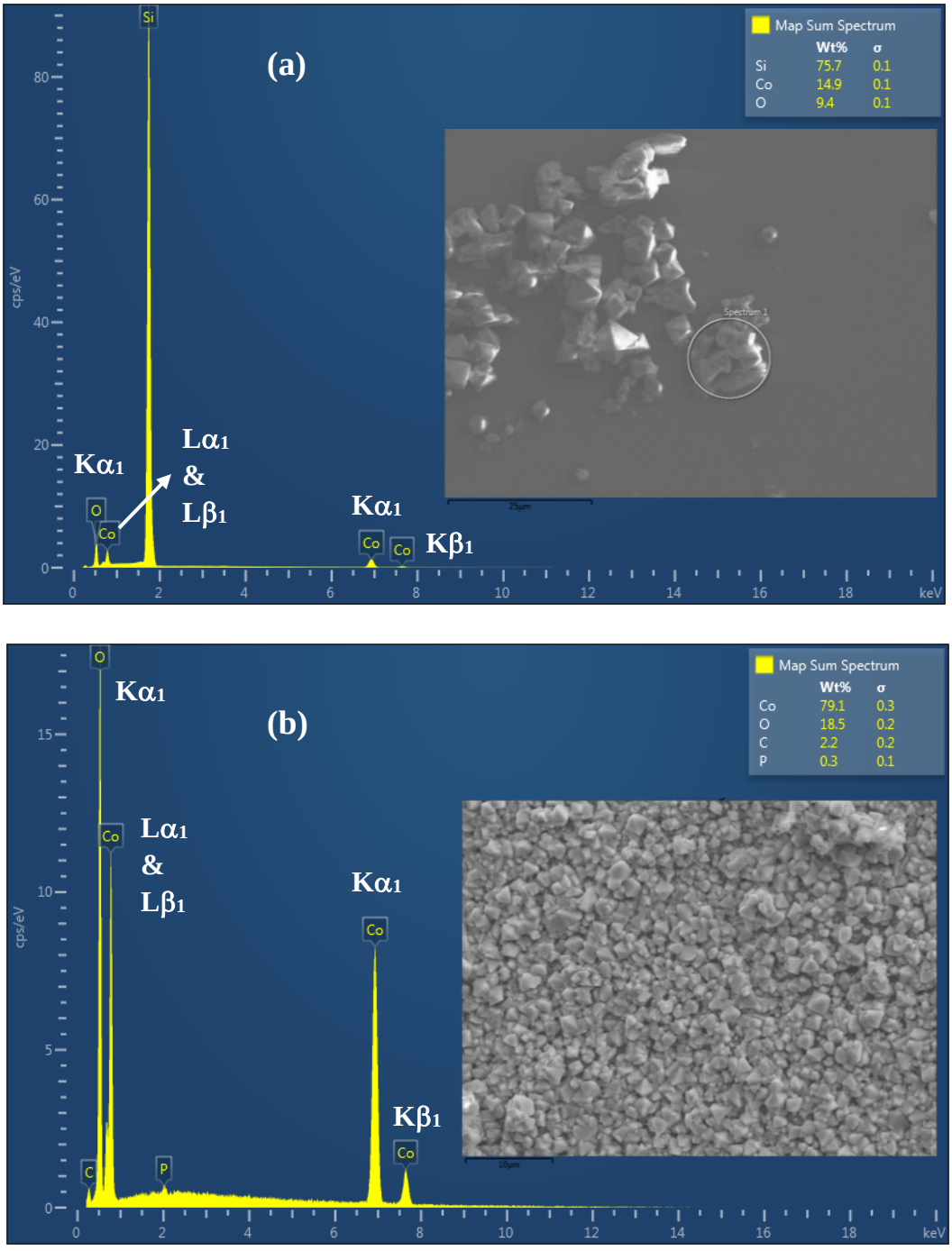

Figure 3.5. Representative EDX spectra for sample #11 (a) and sample #16A (b). The EDXS analysis of the octahedra (shown as insets) shows only cobalt and oxygen peaks whose positions match the literature values listed in Table 3.2. Strong Si peak observed in (a) is from the Si wafer used to mount the sample. Small amounts of carbon and phosphorous observed in (b) could be attributed to teichoic acids from *L. rhamnosus*.

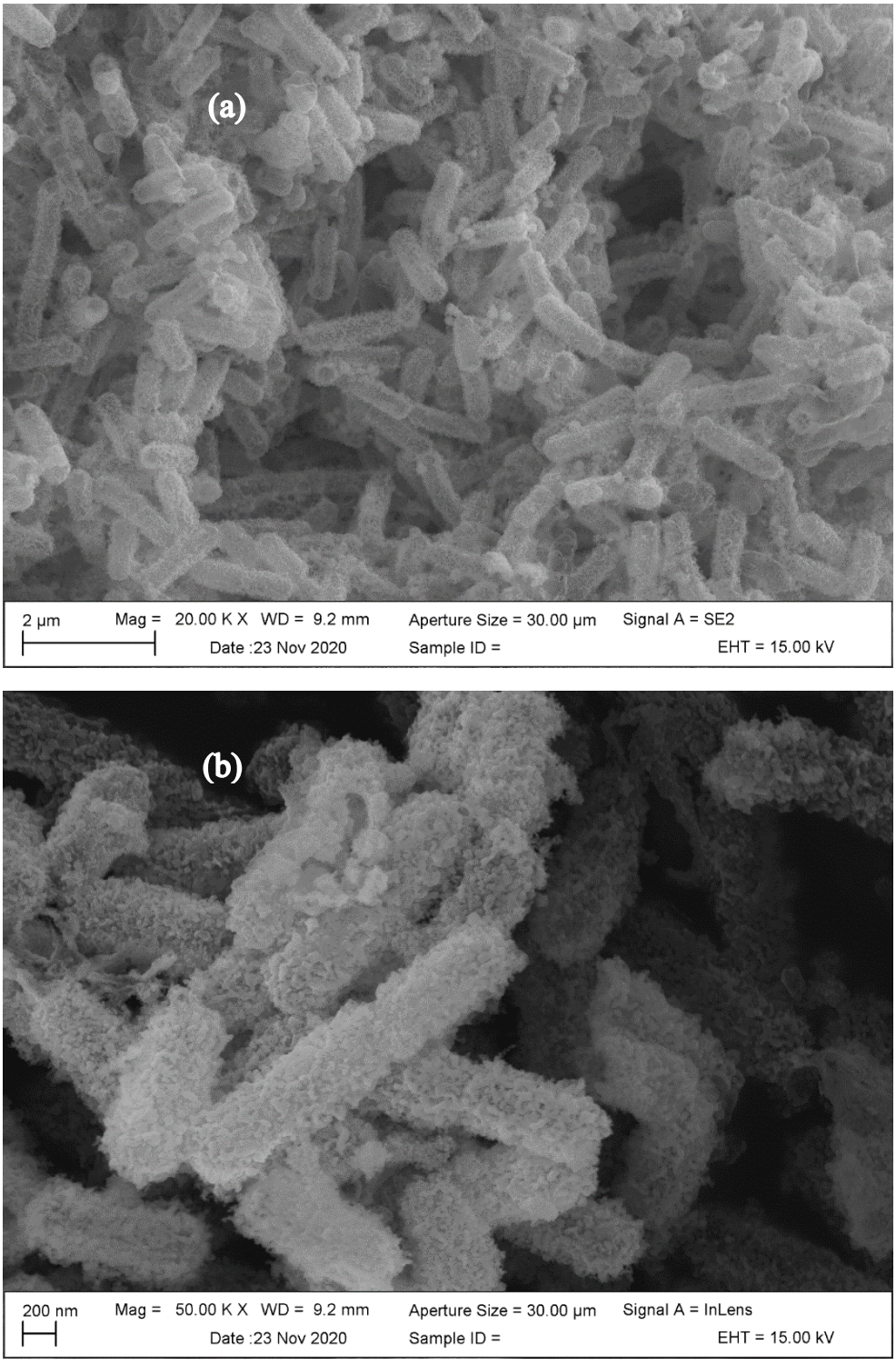

Figure 3.6. The SEM images of sample #15B. (a) shows individual rods of approximately 2 µm in length that match the dimensions of *L. rhamnosus*. (b) Closer look at some of the broken rods reveal hollow structures, supporting the hypothesized electrostatic interaction between Co^{2+} and the teichoic acids resulting in the formation of cobalt oxy-hydroxide layer on the bacterial surface.

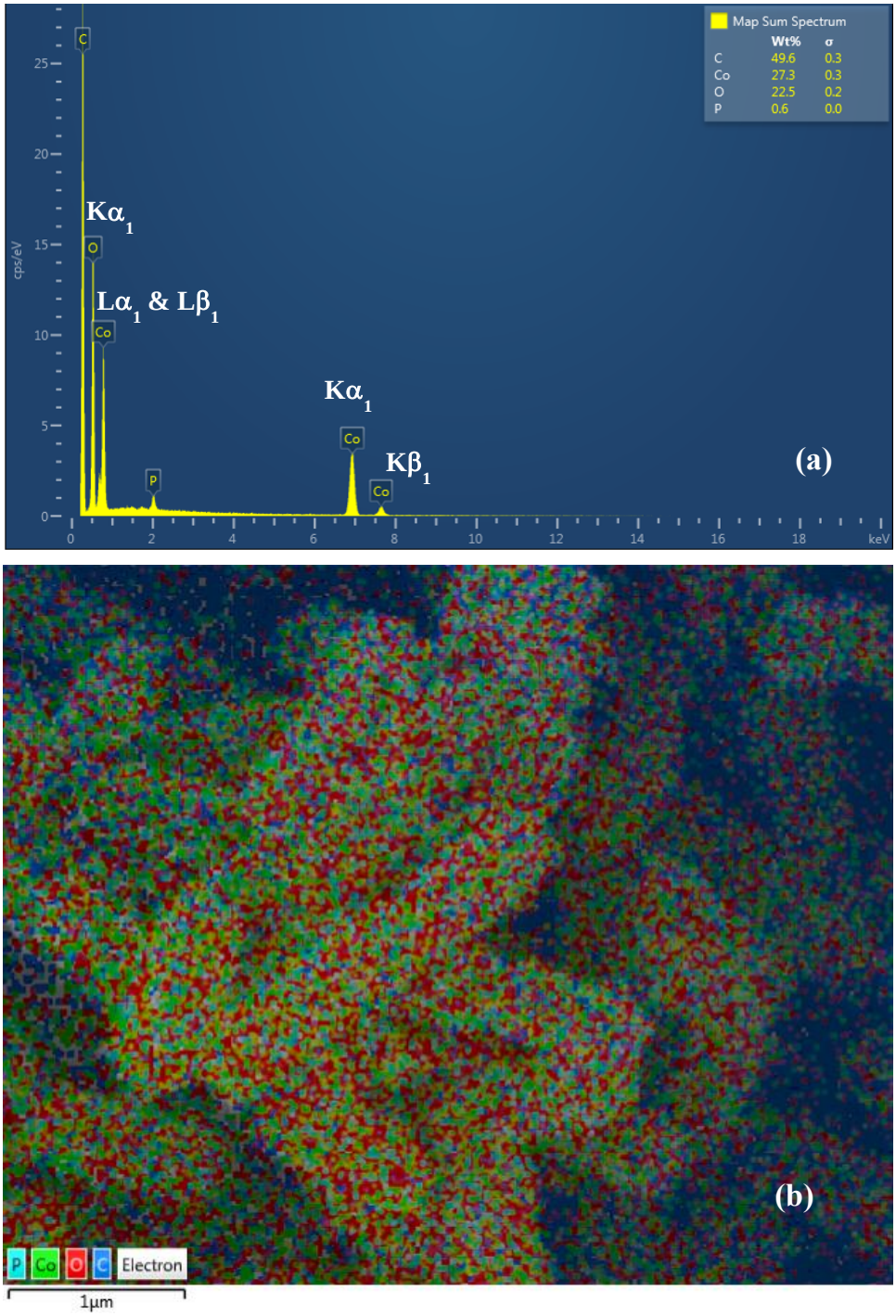

Figure 3.7. (a) The EDX spectrum of calcined sample #15B shows the presence of cobalt and oxygen as the prevalent elements. (b) FE-SEM image showing the elements present with arbitrarily assigned colors. With green representing cobalt and red representing oxygen, it is clear that Co and O make up the bulk of the rod-like structures in the image. Dark-blue dots represent the carbon and can be mainly attributed to the carbon tape used for sample mounting. See text for additional details.

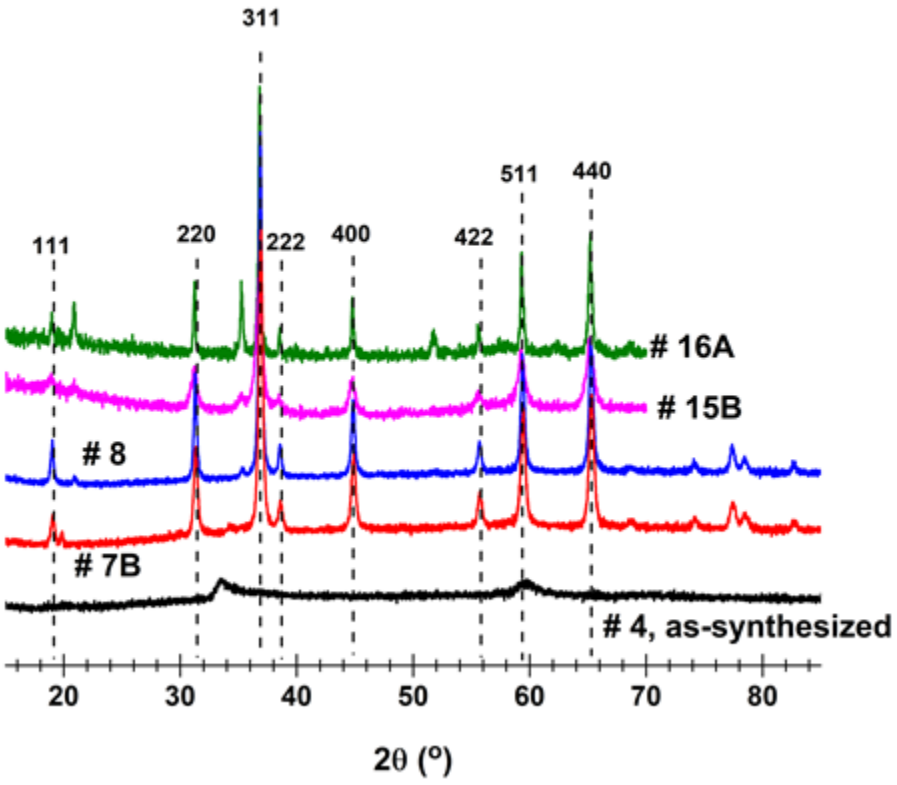

Figure 3.8. Powder XRD spectra of as-synthesized (sample #4, cf. Table S1) and calcined #7B, #8, #15B and #16B samples. While as-synthesized powder is mostly amorphous, the peaks observed in the calcined samples are indicative of cubic spinel structure for Co_3O_4 [14]. See text for additional details.

Representative powder XRD (pXRD) spectra for as-synthesized and calcined powders are depicted in Figure 3.8. While lack of diffraction peaks in as-synthesized powders suggest that they are amorphous in nature, all calcined samples show eight distinct peaks between the angles of 15° - 70°. Comparison of these spectra with literature data[14,25,34] confirm that all the calcined samples crystallize in cubic spinel crystal structure. Sources behind the additional peaks, such as the ones in #7B ($2\theta = 20°$), #8 ($2\theta = 21.5°$), and #16A ($2\theta = 22°$, 35°, 53°), are currently not known. However, we speculate that they might be from other forms of cobalt oxide / cobalt oxy-hydroxides.

To determine if the bacteria are playing a role in the synthesis, a solution of cobalt was mixed with borohydride at a 1:1 molar ratio under the same conditions and parameters as a normal synthesis. The resulting as-synthesized powder was attracted to a magnet, indicating that it is ferromagnetic metallic cobalt. Surprisingly, as seen from the pXRD spectra (data not shown), the metallic cobalt neither crystallized nor oxidized during calcination at 650 °C in air. Nevertheless, this suggests that the bacteria are most likely playing a role in the formation of Co_3O_4.

To evaluate the effect of calcination temperature, samples from initial syntheses were calcined at 200 °C and 300 °C in air (cf. Table S1). However, the pXRD spectra (data not shown) for these samples were not clean enough to confirm the phase identity and purity of Co_3O_4. Therefore, a calcination temperature of 650 °C was chosen because this is a high enough temperature to oxidize cobalt hydroxides/oxy-hydroxides, present in the as-synthesized powders, to Co_3O_4 but is low enough to prevent thermal decomposition of Co_3O_4 to CoO in presence of air[35]. A 12-hour calcination time was selected in response to high levels of noise in the XRD spectra for samples calcined for less time; originally, based on the work of Shim et al.[6], a 6-hour calcination time was used.

The effect of ramp rate on the product quality was also evaluated. Since Co_3O_4 in the cubic spinel structure is the most thermodynamically stable oxide of cobalt, it was assumed that the rate at which temperature was ramped to 650 °C did not have an impact on product formation, as long as the sample was still held at 650 °C for 12 hours. However, these syntheses occasionally produced calcined powders with mixed pink/purple and black coloration (Samples #10 and 12, cf. Table S1). XRD was used to analyze Sample 10 (data not shown), and it revealed the cubic spinel spectrum along with several unknown peaks of comparable intensity. These peaks were not characterized. Since these powders couldn't be separated, their identity couldn't be established with any certainty. Hence, the ramp rate was increased to 12 hours. Since multi-colored calcined samples have not been observed with the new ramp rate, it has been used for all subsequent samples.

The work of Shim et al.[6] suggested a 2:1 molar ratio of Co^{2+} to BH_4^-. Samples #5B and #7B used a 1:1 molar ratio, as did the majority of the past syntheses. Sample #15B was the first to use the 2:1 molar ratio, and it was successful in producing the bacteria-shaped product. While the 1:1 ratio has also yielded the desired morphology, it was determined that a 2:1 molar ratio is better suited to synthesize Co_3O_4 using *L. rhamnosus*.

Peak width analysis of pXRD spectra can provide an estimation of crystallite size, defined as the size of the smallest single-crystal, present in the sample. In case of nanomaterials, this should not be confused with the particle size which represents the overall dimensions of the nanoparticle. The re-arranged Scherrer equation[32], shown in Eq. 1, relates the diffraction peak width to the crystallite size.

$$\cos\theta = \frac{K\lambda}{L}\frac{1}{\beta} \qquad (1)$$

Here, L is the crystallite size, λ is the wavelength of x-ray radiation used to collect the spectra, θ is the diffracted angle of the peak, β is the full width at half maximum (FWHM), and K is a constant that varies from 0.62 – 2.08 and is often referred to as shape factor[32]. As can be seen from Eq. 1, a plot of $\cos\theta$ vs. $(1/\beta)$ should yield a straight line with a slope of $(K\lambda/L)$. Therefore, knowing the values of K and λ, crystallite size L can be estimated.

FWHM values can be obtained from analyzing the peak shape. For sample #15B, in order to prevent over parametrization, only the five most intense pXRD peaks (see Table 3.3) were chosen for peak shape analysis and were fit to a composite function containing five Gaussian functions (cf. Eqs. S1 and S2). While Table 3.3 lists the peak positions and FWHM values, Fig. 3.9 shows the linear fit of cosθ vs. (1/β) data for sample #15B. From a slope of 0.0159 rad^{-1}, crystallite size, *L*, for sample #15B can estimated as 8.62 nm.

Table 3.3. Peak positions (2θ) and FWHM (β) values for sample #15B. cosθ and (1/β) values listed were analyzed using the Scherrer equation shown in Eq.1.

Synthesis	Peak Assignment	2θ (Deg)	cosθ	β = FWHM (Rad)	1/β (Rad^{-1})
15B	220	31.18091	0.993104	0.0121264	82.465018
	311	36.77407	0.89493	0.012056	82.946041
	400	44.74968	0.927289	0.0092181	108.48179
	511	59.28653	0.200497	0.0160802	62.188378
	440	65.17645	0.388034	0.0147503	67.795183

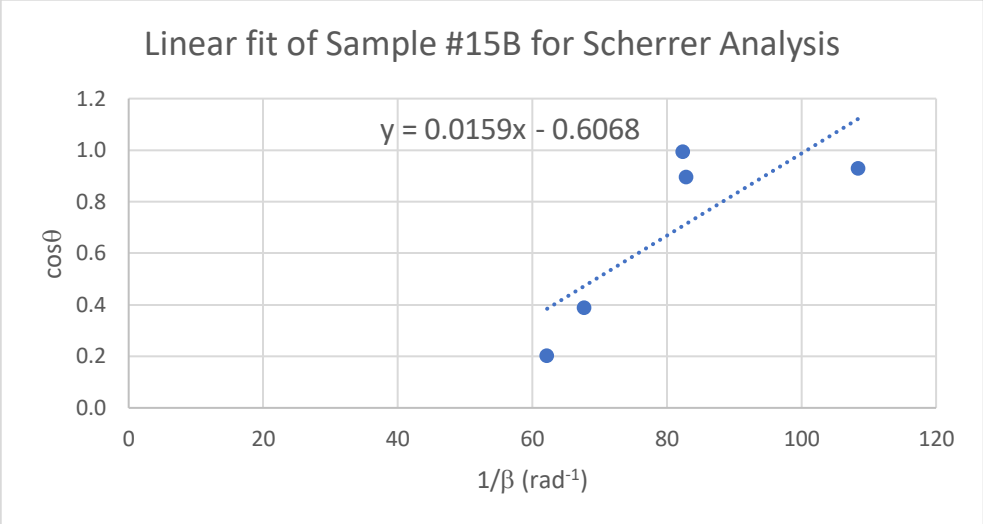

Figure 3.9. A plot of cosθ vs. (1/β) for sample #15B. Dotted line represents the linear fit to Scherrer equation shown in Eq.1. Crystallite size was estimated from the slope as 8.62 nm. See text for more details.

In this calculation, K = 0.89 (representative of spherical crystals with cubic symmetry) and λ = 0.154 nm (for Cu K_α radiation used for pXRD measurements) were used. It should be noted that crystallite size estimate here is highly qualitative because of the assumption invoked about the shape of the crystallites in #15B and potential errors from peak shape analysis due to poor baseline and signal to noise ratio (See Fig. S1). Additional reasons include: (a) dependence of K on, besides the shape of the crystallite, the crystallite size distribution as well as FWHM estimation method[32], (b) contributions to peak width, β, from factors such as instrument, lattice strain and lattice defects[32], and (c) validity of Scherrer equation is true for crystallite sizes only up to ~100 nm[32]. Therefore, complex models are required to theoretically estimate the crystallite sizes[32] and Transmission electron microscopy measurements are required to experimentally confirm them.

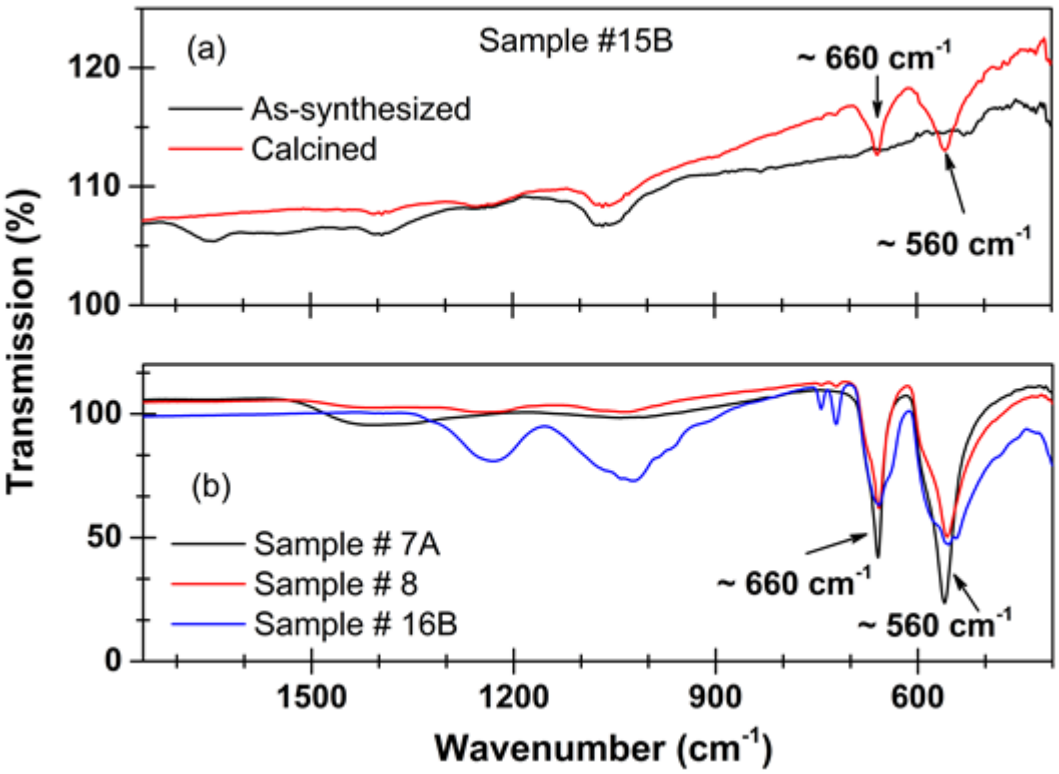

Figure 3.10. FTIR spectra of (a) as-synthesized and calcined samples from synthesis 15B, and (b) calcined samples from syntheses 7A, 8 and 16B. The peaks observed at ~ 560 cm^{-1} and ~ 660 cm^{-1} correspond to Co – O vibrational frequencies of Co_3O_4 [33]. See Table 3.1 for synthesis conditions of these samples and text for additional details.

FT-IR spectra were collected to identify the vibrational frequencies of Co – O bonds in as-synthesized and calcined samples. While Figure 3.10.a shows the FT-IR spectra for as-synthesized and calcined powders for sample #15B, Figure 3.10.b depicts the representative FT-IR spectra for the calcined powders of samples #7A, #8 and #16B. As

can be seen from the figure, it is clear that calcined powders consistently show distinct peaks that correspond Co – O vibrations. Specifically, the peak at ~660 cm^{-1} is attributed to vibrations of the Co^{3+} — O bond, and the peak at ~ 560 cm^{-1} corresponds to vibration of the Co^{2+}—O bond[34]. The additional peaks observed in both as-synthesized and calcined samples could be attributed to carbon-based vibrational modes from Tween-80 or capping agents like PEG or LTAs in *L. rhamnosus*. Based on the EDX and FT-IR data, along with the fact that Co_3O_4 crystallizes only in the cubic spinel structure, it can be reasonably concluded that calcination of various colored as-synthesized powders in air at 650 °C produces Co_3O_4 nanocrystals.

3.2. Zeta potential measurements

The zeta potential can be loosely defined as a measure of the charge on the surface of the bacteria. Literature reports a zeta potential of −41 mV in DI water for *B. subtilis* [36], while the zeta potential of *L. rhamnosus* is reported to be between −10 mV and −12 mV[37]. Since the bacterial species was changed from *B. subtilis* to *L. rhamnosus* for this project, the zeta potential for each species was recorded and compared to literature values. In DI water, the potential of *B. subtilis* was measured at −49.6 mV, and the potential of *L. rhamnosus* in DI water was measured at −18.0 mV. The zeta potential spectra for each can be found in Figure S2. As mentioned in section 2.2.6, the zeta potential is expected to depend on the pH and ionic strengths of a solution and since they are not currently available, the observed differences from the literature cannot be explained at this point. However, our data is in qualitative agreement with previously reported differences in surface charge between the two species. This can be understood in terms of the differences in their cell wall structures namely, while *B. subtilis* has both LTAs and WTAs, *L. rhamnosus* has only LTAs. As demonstrated in this project, an average surface charge of −18.0 mV on *L. rhamnosus* still proved effective for the production of Co_3O_4 nanostructures.

3.3. Proposed mechanism

Shim *et al.*[6] suggested that the mechanism relies on the teichoic acids of the bacteria. The teichoic acids cover the entire surface of the most Gram-positive bacteria and are rich in negatively charged phosphate groups. In nature, bacteria in the soil use D-alanine to help reduce their surface charge and prevent the adsorption of cations like Mg^{2+} found naturally in the soil through a process simply called D-Alanylation[38–41]. If the teichoic acids are coordinating the adhesion of Co^{2+} to the bacterial surface, that could explain why large chunks of cobalt oxide were seen on the surface of the rods in Figure 3.3.

We propose that, as a first-step the positively charged Co^{2+} is electrostatically coordinated to the negatively charged bacterial surface, and the added BH_4^- reduces the Co^{2+} to metallic cobalt. Metallic cobalt (dark gray or black in color) spontaneously re-oxidizes in solution under atmospheric conditions, most likely, to a cobalt oxy-hydroxide ($Co_xO_y(OH)_z$), which coats the bacterial surface. This would explain why the solution initially turns black upon

addition of borohydride then gradually changes to green, blue, brown, gray, purple, etc. Finally, upon calcination in air the cobalt oxy-hydroxide coating the bacteria transforms to the most thermodynamically stable cobalt oxide, namely Co_3O_4 ($\Delta_f G°$ ~ –910 kJ/mol @ 25°C) in a crystalline form. Our experiments show that without the bacteria in solution, the reduced cobalt stays in the metallic state and doesn't re-oxidize in solution under the same atmospheric conditions.

4. Summary and future directions

4.1. Summary

Work presented in this thesis shows that by introducing Co^{2+} to a suspension of *L. rhamnosus*, followed by a reaction with BH_4^- and a calcination at 650 °C, it is possible to produce Co_3O_4 rods that match the morphology of the bacterial template. This is supported by SEM, pXRD and EDXS measurements.

The implications of this conclusion are significant in several ways. There is now further evidence supporting an inexpensive and comparatively safe method for Co_3O_4 nanomaterial production. Additionally, the mechanism of formation, if it can be conclusively attributed to the negative charge of teichoic acids, would allow for production of other metal oxides using *L. rhamnosus*. Further, because nearly all Gram-positive bacteria have teichoic acids, the mechanism could be extended to other Gram-positive bacteria of different morphologies, thus giving researches the ability to customize the synthesis of metal oxides with various morphologies and properties to suit the desired applications.

4.2. Future directions

While the outcomes from this work are significant, there are still several aspects that remain unexplored and unanswered. The mechanism's hypothesized reliance on teichoic acids is one such aspect. Their role could be made clearer through two experiments: first, if a mutant of *L. rhamnosus* were to be used in the synthesis, specifically with knock-out mutations of teichoic acid synthesis, the negative surface charge of the bacteria would be diminished and thus it could be assumed that the formation of Co_3O_4 would be reduced. Alternately, as Gram-positive bacteria often use D-alanine to reduce the charge on their teichoic acids to prevent soil-based metals from affixing, it should also be possible to introduce D-alanine to the growth media to reduce the surface charge.

Another experiment yet to be performed tests the hypothesized spontaneous re-oxidation of Co^0 to Co^{2+} and Co^{3+}. If the synthesis were to be carried out by removing oxygen from the solution by bubbling Ar or N_2 through it, it should not be possible for Co^0 to oxidize. That being said, if the Co^0 were oxidizing with free hydroxyl groups from the aqueous solution, removing the oxygen in solution would not have any impact on this type of re-oxidation. Another aspect of the spontaneous re-oxidation yet to be determined is whether the bacteria play a role in coordinating Co^{2+} or if the reducing agent reacts with Co^{2+} in solution before anything affixes to the bacteria. To test this, metallic cobalt can be introduced directly to the bacterial suspension; if nothing happens, it would suggest the Co^{2+} first affixes to the bacteria and is then reduced and re-oxidized.

Finally, after the previous questions have been answered, the experiment could be extended to other bacterial species and other metal oxides. This is ultimately the long-term goal of this project, as it would have the widest impacts in the many fields exploring applications of metal oxides.

5. References

(1) Akbarzadeh, A.; Samiei, M.; Davaran, S. Magnetic Nanoparticles: Preparation, Physical Properties, and Applications in Biomedicine. *Nanoscale Res. Lett.* **2012**, *7*. https://doi.org/10.1186/1556-276X-7-144.

(2) Pankhurst, Q. A.; Connolly, J.; Jones, S. K.; Dobson, J. *Applications of Magnetic Nanoparticles in Biomedicine*; 2003; Vol. 36.

(3) Spaldin, N. A. *Magnetic Materials: Fundamentals and Applications*, 2nd Editio.; The Press Syndicate of the University of Cambridge: Cambridge, United Kingdom.

(4) Jungwirth, T.; Marti, X.; Wadley, P.; Wunderlich, J. Antiferromagnetic Spintronics. *Nature Nanotechnology*. 2016. https://doi.org/10.1038/nnano.2016.18.

(5) Fernandez-Garcia, M.; Rodriguez, J. A. *Metal Oxide Nanoparticles*; Brookhaven National Laboratory: Upton, NY, 2007; Vol. 3.

(6) Shim, H. W.; Jin, Y. H.; Seo, S. D.; Lee, S. H.; Kim, D. W. Highly Reversible Lithium Storage in Bacillus Subtilis-Directed Porous Co3O4 Nanostructures. *ACS Nano* **2011**, *5* (1), 443–449. https://doi.org/10.1021/nn1021605.

(7) Gao, M.; Wang, W. K.; Rong, Q.; Jiang, J.; Zhang, Y. J.; Yu, H. Q. Porous ZnO-Coated Co 3 O 4 Nanorod as a High-Energy-Density Supercapacitor Material. *ACS Appl. Mater. Interfaces* **2018**, *10* (27), 23163–23173. https://doi.org/10.1021/acsami.8b07082.

(8) Zhao, J.; Chen, Z.; Zhou, G.; Li, F.; Ren, W.; Wen, L.; Gao, L.; Wu, Z.-S.; Cheng, H.-M. Graphene Anchored with Co 3 O 4 Nanoparticles as Anode of Lithium Ion Batteries with Enhanced Reversible Capacity and Cyclic Performance . *ACS Nano* **2010**, *4* (6), 3187–3194. https://doi.org/10.1021/nn100740x.

(9) Wang, Y.; Fan, S.; Wu, S.; Wang, C.; Huang, Z.; Zhang, L. In Situ Synthesis and Unprecedented Electrochemical Performance of Double Carbon Coated Cross-Linked Co 3 O 4. *ACS Appl. Mater. Interfaces* **2018**, *10* (49), 42372–42379. https://doi.org/10.1021/acsami.8b15604.

(10) Pocoví-Martínez, S.; Zumeta-Dube, I.; Diaz, D. Production of Methanol from Aqueous CO 2 by Using Co 3 O 4 Nanostructures as Photocatalysts. *J. Nanomater.* **2019**, *2019*, 1–10. https://doi.org/10.1155/2019/6461493.

(11) Shi, W.; Chopra, N. Controlled Fabrication of Photoactive Copper Oxide-Cobalt Oxide Nanowire Heterostructures for Efficient Phenol Photodegradation. *ACS Appl. Mater. Interfaces* **2012**, *4* (10), 5590–5607. https://doi.org/10.1021/am301488c.

(12) Meier, F.; Levy, J.; Loss, D. Quantum Computing with Antiferromagnetic Spin Clusters. *Phys. Rev. B - Condens. Matter Mater. Phys.* **2003**, *68* (13). https://doi.org/10.1103/PhysRevB.68.134417.

(13) Wang, K.; Cao, Y.; Hu, J.; Li, Y.; Xie, J.; Jia, D. Solvent-Free Chemical Approach to Synthesize Various Morphological Co3O4 for CO Oxidation. *ACS Appl. Mater. Interfaces*

2017. https://doi.org/10.1021/acsami.7b01142.

(14) Goudarzi, M.; Salavati-Niasari, M. Synthesis, Characterization and Evaluation of Co3O4 Nanoparticles Toxicological Effect; Synthesized by Cochineal Dye via Environment Friendly Approach. *J. Alloys Compd.* **2019**. https://doi.org/10.1016/j.jallcom.2019.01.028.

(15) Dong, Y.; He, K.; Yin, L.; Zhang, A. A Facile Route to the Controlled Synthesis of Co3O4 Nanoparticles. *Nanotechnology* **2007**, *18* (43), 435602 (all pages).

(16) Hebbalalu, D.; Lalley, J.; Nadagouda, M. N.; Varma, R. S. Greener Techniques for the Synthesis of Silver Nanoparticles Using Plant Extracts, Enzymes, Bacteria, Biodegradable Polymers, and Microwaves. *ACS Sustainable Chemistry and Engineering*. July 1, 2013, pp 703–712. https://doi.org/10.1021/sc4000362.

(17) Yadav, V. S. K.; Purkait, M. K. Electrochemical Studies for CO2 Reduction Using Synthesized Co3O4 (Anode) and Cu2O (Cathode) as Electrocatalysts. *Energy and Fuels* **2015**, *29* (10), 6670–6677. https://doi.org/10.1021/acs.energyfuels.5b01656.

(18) Bharde, A. A.; Parikh, R. Y.; Baidakova, M.; Jouen, S.; Hannoyer, B.; Enoki, T.; Prasad, B. L. V.; Shouche, Y. S.; Ogale, S.; Sastry, M. Bacteria-Mediated Precursor-Dependent Biosynthesis of Superparamagnetic Iron Oxide and Iron Sulfide Nanoparticles. *Langmuir* **2008**, *24* (11), 5787–5794. https://doi.org/10.1021/la704019p.

(19) Vennela, A. B.; Mangalaraj, D.; Muthukumarasamy, N.; Agilan, S.; Hemalatha, K. V. Structural and Optical Properties of Co 3 O 4 Nanoparticles Prepared by Sol-Gel Technique for Photocatalytic Application. *Int. J. Electrochem. Sci.* **2019**, *14* (4), 3535–3552. https://doi.org/10.20964/2019.04.40.

(20) Zhu, H. T.; Luo, J.; Liang, J. K.; Rao, G. H.; Li, J. B.; Zhang, J. Y.; Du, Z. M. Synthesis and Magnetic Properties of Antiferromagnetic Co3O4 Nanoparticles. *Phys. B Condens. Matter* **2008**. https://doi.org/10.1016/j.physb.2008.03.024.

(21) Qiao, L.; Xiao, H. Y.; Meyer, H. M.; Sun, J. N.; Rouleau, C. M.; Puretzky, A. A.; Geohegan, D. B.; Ivanov, I. N.; Yoon, M.; Weber, W. J.; et al. Nature of the Band Gap and Origin of the Electro-/Photo-Activity of Co3O4. *J. Mater. Chem. C* **2013**, *1* (31), 4628–4633. https://doi.org/10.1039/c3tc30861h.

(22) He, T.; Chen, D.; Jiao, X.; Wang, Y.; Duan, Y. Solubility-Controlled Synthesis of High-Quality Co3O4 Nanocrystals. *Chem. Mater.* **2005**, *17* (15), 4023–4030. https://doi.org/10.1021/cm050727s.

(23) Feng, J.; Zeng, H. C. Size-Controlled Growth of Co3O4 Nanocubes. *Chem. Mater.* **2003**. https://doi.org/10.1021/cm020940d.

(24) Hwa, Y.; Kim, W. S.; Yu, B. C.; Hong, S. H.; Sohn, H. J. Enhancement of the Cyclability of a Si Anode through Co3O 4 Coating by the Sol-Gel Method. *J. Phys. Chem. C* **2013**, *117* (14), 7013–7017. https://doi.org/10.1021/jp401333v.

(25) Al-Tuwirqi, R.; Al-Ghamdi, A. A.; Aal, N. A.; Umar, A.; Mahmoud, W. E. Facile Synthesis and Optical Properties of Co3O4 Nanostructures by the Microwave Route. *Superlattices Microstruct.* **2011**, *49* (4), 416–421. https://doi.org/10.1016/j.spmi.2010.12.010.

(26) Diallo, A.; Beye, A. C.; Doyle, T. B.; Park, E.; Maaza, M. Green Synthesis of Co3O4 Nanoparticles via Aspalathus Linearis: Physical Properties. *Green Chemistry Letters and Reviews*. 2015, pp 30–36. https://doi.org/10.1080/17518253.2015.1082646.

(27) Ikhuoria, E. U.; Omorogbe, S. O.; Sone, B. T.; Maaza, M. Bioinspired Shape Controlled Antiferromagnetic Co3O4 with Prism Like-Anchored Octahedron Morphology: A Facile Green Synthesis Using Manihot Esculenta Crantz Extract. *Science and Technology of Materials*. 2018. https://doi.org/10.1016/j.stmat.2018.02.003.

(28) Imamura, D.; Kuwana, R.; Takamatsu, H.; Watabe, K. Localization of Proteins to Different Layers and Regions of Bacillus Subtilis Spore Coats. *J. Bacteriol.* **2010**, *192* (2), 518–524. https://doi.org/10.1128/JB.01103-09.

(29) Stragier, P.; Losick, R. Molecular Genetics of Bacteria. *Biochem. Educ.* **2003**, *17* (4), 221. https://doi.org/10.1016/0307-4412(89)90170-2.

(30) Crow, V.; Curry, B. *Lactobacillus Spp.: Other Species*; 2011; Vol. 3.

(31) Maass, S.; Sievers, S.; Zühlke, D.; Kuzinski, J.; Sappa, P. K.; Muntel, J.; Hessling, B.; Bernhardt, J.; Sietmann, R.; Völker, U.; et al. Efficient, Global-Scale Quantification of Absolute Protein Amounts by Integration of Targeted Mass Spectrometry and Two-Dimensional Gel-Based Proteomics. *Anal. Chem.* **2011**, *83* (7), 2677–2684. https://doi.org/10.1021/ac1031836.

(32) Rabiei, M.; Palevicius, A.; Monshi, A.; Nasiri, S.; Vilkauskas, A.; Janusas, G. Comparing Methods for Calculating Nano Crystal Size of Natural Hydroxyapatite Using X-Ray Diffraction. *Nanomaterials* **2020**, *10* (9), 1–21. https://doi.org/10.3390/nano10091627.

(33) Yadav, V. S. K.; Purkait, M. K. Electrochemical Studies for CO2 Reduction Using Synthesized Co3O4 (Anode) and Cu2O (Cathode) as Electrocatalysts. *Energy and Fuels* **2015**, *29* (10), 6670–6677. https://doi.org/10.1021/acs.energyfuels.5b01656.

(34) Xu, H.; Hai, Z.; Diwu, J.; Zhang, Q.; Gao, L.; Cui, D.; Zang, J.; Liu, J.; Xue, C. Synthesis and Microwave Absorption Properties of Core-Shell Structured Co3O4-PANI Nanocomposites. *J. Nanomater.* **2015**, *2015* (October). https://doi.org/10.1155/2015/845983.

(35) Gazulla, M. F.; Ventura, M. J.; Andreu, C. Characterization of Cobalt Oxides Transformations with Temperature at Different Atmospheres. *Int. J. Chem. Sci. Res.* **2019**, *17* (3), 312.

(36) Pajerski, W.; Ochonska, D.; Brzychczy-Wloch, M.; Indyka, P.; Jarosz, M.; Golda-Cepa, M.; Sojka, Z.; Kotarba, A. Attachment Efficiency of Gold Nanoparticles by Gram-Positive and Gram-Negative Bacterial Strains Governed by Surface Charges. *J. Nanoparticle Res.* **2019**, *21* (8). https://doi.org/10.1007/s11051-019-4617-z.

(37) Deepika, G.; Green, R. J.; Frazier, R. A.; Charalampopoulos, D. Effect of Growth Time on the Surface and Adhesion Properties of Lactobacillus Rhamnosus GG. *J. Appl. Microbiol.* **2009**, *107* (4), 1230–1240. https://doi.org/10.1111/j.1365-2672.2009.04306.x.

(38) Abi Khattar, Z.; Rejasse, A.; Destoumieux-Garzón, D.; Escoubas, J. M.; Sanchis, V.; Lereclus, D.; Givaudan, A.; Kallassy, M.; Nielsen-Leroux, C.; Gaudriault, S. The Dlt

Operon of Bacillus Cereus Is Required for Resistance to Cationic Antimicrobial Peptides and for Virulence in Insects. *J. Bacteriol.* **2009**, *191* (22), 7063–7073. https://doi.org/10.1128/JB.00892-09.

(39) Valik, Ľ.; Lipatkova, D. M. A. Characterization of the Growth of Lactobacillus Rhamnosus GG.Pdf. *J. food Nutr. Res.* **2008**, *47* (2), 60–67.

(40) Lambert, P. A.; Hancock, I. C.; Baddiley, J. The Interaction of Magnesium Ions with Teichoic Acid. *Biochem. J.* **1975**, *149* (3), 519–524.

(41) Romaniuk, J. A. H.; Cegelski, L. Peptidoglycan and Teichoic Acid Levels and Alterations in Staphylococcus Aureus by Cell-Wall and Whole-Cell Nuclear Magnetic Resonance. *Biochemistry* **2018**, *57* (26), 3966–3975. https://doi.org/10.1021/acs.biochem.8b00495.

Supplementary Tables and Figures

Table S1. The summary of parameters for each synthesis. The Notes column indicates procedural alterations, abnormal or notable results.

Synthesis Number	Lactobacillus Optical Density (@ 600 nm)	Resuspended in	$CoCl_2$ moles	$NaBH_4$ moles	Other Compound and Moles	Cobalt Addition Rate	Time with Co^{2+}	Reducing Agent Addition Rate	Time with Reducing Agent	Solution Color	Calcination Ramp Rate	Notes
1A	Not Recorded	DI water	0.01	0.0125		10 mL/min	45 min	10 mL/min	23.5 H	Black	6 H to 200 °C	
1B	Not Recorded	DI water	0.01	0.0125		10 mL/min	45 min	10 mL/min	48 H	Black	6 H to 300 °C	
2A	>2.0	DI water	0.00683	0.00497		10 mL/min	30 min	10 mL/min	24 H	Brown/Green	6 H to 300 °C	
2B	>2.0	DI water	0.00683	0.00497		10 mL/min	30 min	10 mL/min	96 H	Brown/Green	6 H to 300 °C	
3A	Not Recorded	DI water	0.00683	0.00625		Instant	18 H	10 mL/min	11 Days	Black + Brown	6 H to 300 °C	After calcination, half was recalcined
3B	Not Recorded	DI water	0.00683	0.00625		Instant	11 Days	10 mL/min	18 H	Blue + Pink	6 H to 300 °C	
4	Not Recorded	0.25 M NaCl	0.00625	0.00625		10 mL/min	3.5 H	10 mL/min	30 min	Blue	11 H to 350 °C	
5A	0.5	DI water	0.00683	0.00625		Instant	1 H	10 mL/min	20 H	Black	2 H to 650 °C	Responsive to magnet
5B	0.1	DI water	0.00683	0.00625		Instant	1 H	10 mL/min	20 H	Green	2 H to 650 °C	
5C	0.5	DI water	0.00683	0.00625		Instant	1 H	10 mL/min	20 H	Green	2 H to 650 °C	
5D	1.0	DI water	0.00683	0.00625		Instant	1 H	10 mL/min	20 H	Green	2 H to 650 °C	
6A	Not Recorded	DI water	0.00313	0.0031		Instant	12 H	10 mL/min	48 H	Not Recorded	2 H to 650 °C	
6B	Not Recorded	DI water	0.00313	0.0031		Instant	12 H	10 mL/min	48 H	Not Recorded	2 H to 650 °C	
7A	0.5	DI water	0.00625	0.00625		Instant	24 H	10 mL/min	18 H	Green	3 H to 650 °C	
7B	0.5	0.1 vol % Tween 80	0.00625	0.00625		Instant	24 H	10 mL/min	18 H	Brown/Green	3 H to 650 °C	
7C	0.5	DI water	0.00625	0.00625		Instant	24 H	10 mL/min	18 H	Green	3 H to 650 °C	
7D	0.5	0.1 vol % Tween 80	0.00625	0.00625		Instant	24 H	10 mL/min	18 H	Blue	3 H to 650 °C	
8A	1.931	0.1 vol % Tween 80	0.0055	0.005		5 mL/min	1 H	5 mL/min	16 H	Brown/Green	3 H to 650 °C	Was supposed to be 0.01 mol $CoCl_2$ but the wrong MM was used
8B	0.406	0.1 vol % Tween 80	0.0005	0.0005		5 mL/min	1 H	5 mL/min	16 H	Yellow	N/A	Did not produce enough powder to isolate
9	Not Recorded	0.1 vol % Tween 80	0.0055	0.005		10 mL/min	None	10 mL/min	72 H	Brown/Green	3 H to 650 °C	
11	1.467	0.05 vol % Tween 80	0.022	0.02		10 mL/min	None	10 mL/min	24 H	Dark Green	3 H to 650 °C	Washed with IPA in sonicator, split after calcination, half stirred in IPA for 15 H and half in same with three drops of Tween 80
12A	1.14	0.1 vol % Tween 80	0.0063	0.0125		Instant	36 H	10 mL/min	20 H	Green	3 H to 650 °C	Powders were completely purple after calcination
12B	1.14	0.1 vol % Tween 80	0.0063	0.0063		Instant	36 H	10 mL/min	20 H	Dark Gray	3 H to 650 °C	
13A	1.473	DI water	0.0137	0.131		10 mL/min	72 H	10 mL/min	36 H	Green	12 H to 650 °C	Solution was split three ways immediately before addition on NaBH4, citrate seemed to have no effect on 13C so .131 mol NaBH4 was added and allowed to spin for 48 H. No changes
13B				0.0629				10 mL/min	36 H	Black	12 H to 650 °C	
13C				None	Citrate - 0.131			10 mL/min	36 H	Pink	12 H to 650 °C	
14A	1.440	DI water	0.0137	0.0313		10 mL/min	36 H	10 mL/min	120 H	Green	12 H to 650 °C	Powder was split three ways, one left as-is, one receiving citrate and one receiving PVP as a capping agent
14B				0.0313				10 mL/min	120 H	Green	12 H to 650 °C	
15A	0.5	DI water	0.0033	0.0033		10 mL/min	68 H	10 mL/min	45 H	Gray-Pink	12 H to 650 °C	Powder was very fine, Buchner did not work to isolate
15B	0.5	DI water	0.0033	0.0017		10 mL/min	68 H	10 mL/min	45 H	Brown/Green	12 H to 650 °C	
15C	1.5	DI water	0.01	0.005	PVP - 1.75 g	10 mL/min	68 H	10 mL/min	45 H	Orange/Pink	12 H to 650 °C	Powder was very fine, Buchner did not work to isolate
15D	1.7	DI water	0.01	0.01	L-Alanine - 0.02	10 mL/min	45 H	10 mL/min	72 H		12 H to 650 °C	0.005 mol BH_4^- did not work, so another 0.005 mol were added
16A	1.995	DI water	0.005	0.005		Instant	48 H	10 mL/min	48 H	Light Brown	12 H to 650 °C	After calcination, PEG and powder 16B were added to a flask in 1:1 mass ratio and spun in 100 mL DI water for ~5 H, then isolated and dried
16B	1.995	DI water	0.005	0.005	PEG - 1.1 g	Instant	48 H	10 mL/min	48 H	Light Brown	12 H to 650 °C	

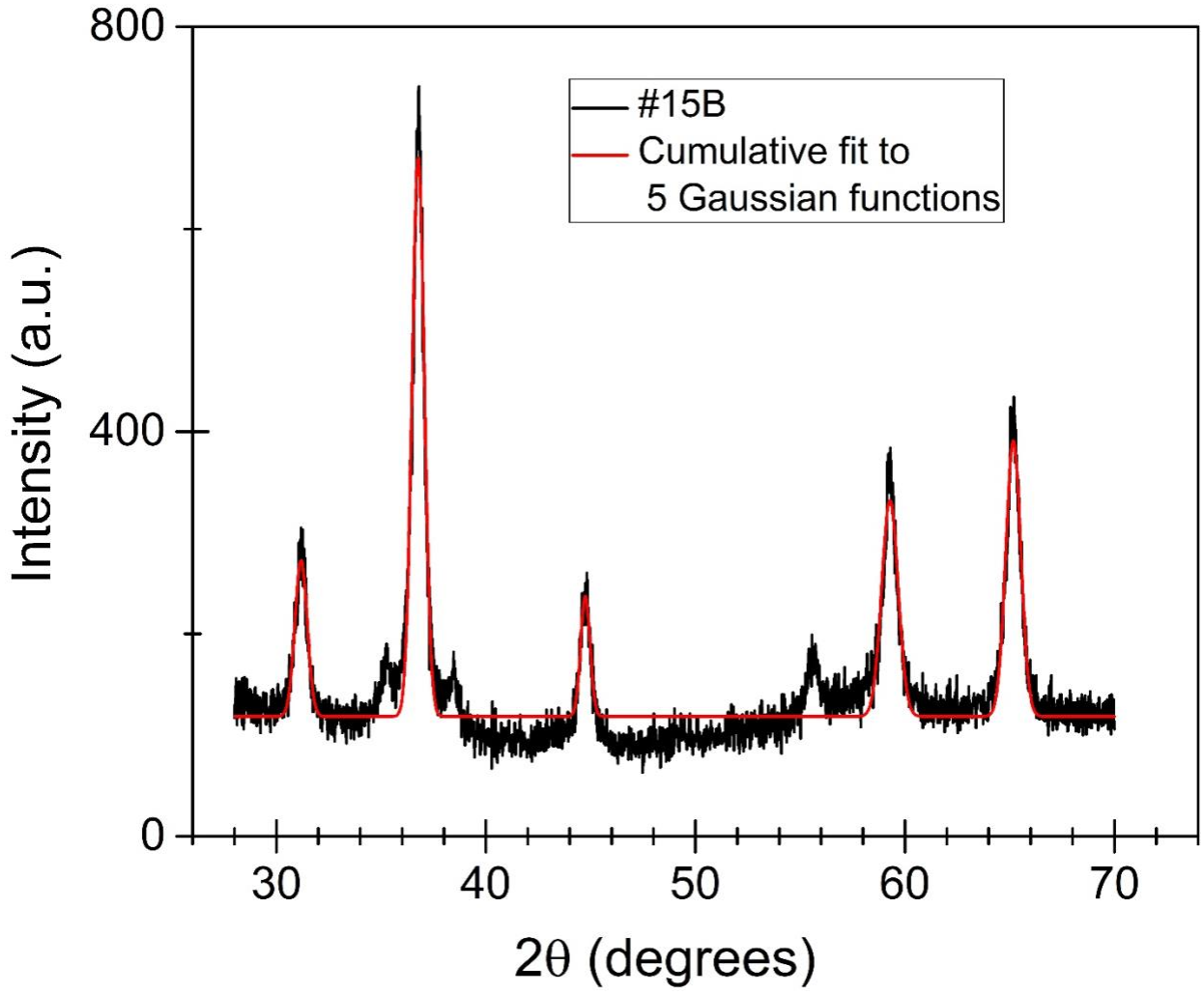

Figure S1. Peak shape analysis of pXRD spectrum of sample #15B. Black curve represents the experimental spectrum and red solid line represents the cumulative fit to five Gaussian functions (see Eq. S1). R^2 value was found to be 0.9194

$$\underline{\text{Gaussian function}}: \quad y_i = y_{0,i} + \frac{A_i}{w_i\sqrt{\pi/2}}\, e^{-2\frac{(x-x_{c,i})^2}{w_i^2}} \qquad \text{(S1)}$$

Here, $y_{0,i}$ is the y-offset for ith peak, $x_{c,i}$ is the center of the ith peak, w_i is the width of the ith peak and A_i is the area of the ith peak. The composite function representing the red line in Fig. S1 is given as:

$$y_{\text{tot}} = \sum_{i=1}^{i=5} y_i \qquad \text{(S2)}$$

Fit procedure: The red line in Fig. S1 is generated by performing a non-linear regression fit of the most intense peaks to Eq. S2 while varying $\{y_0, x_c, w, A_i\}$ for each of the peaks.

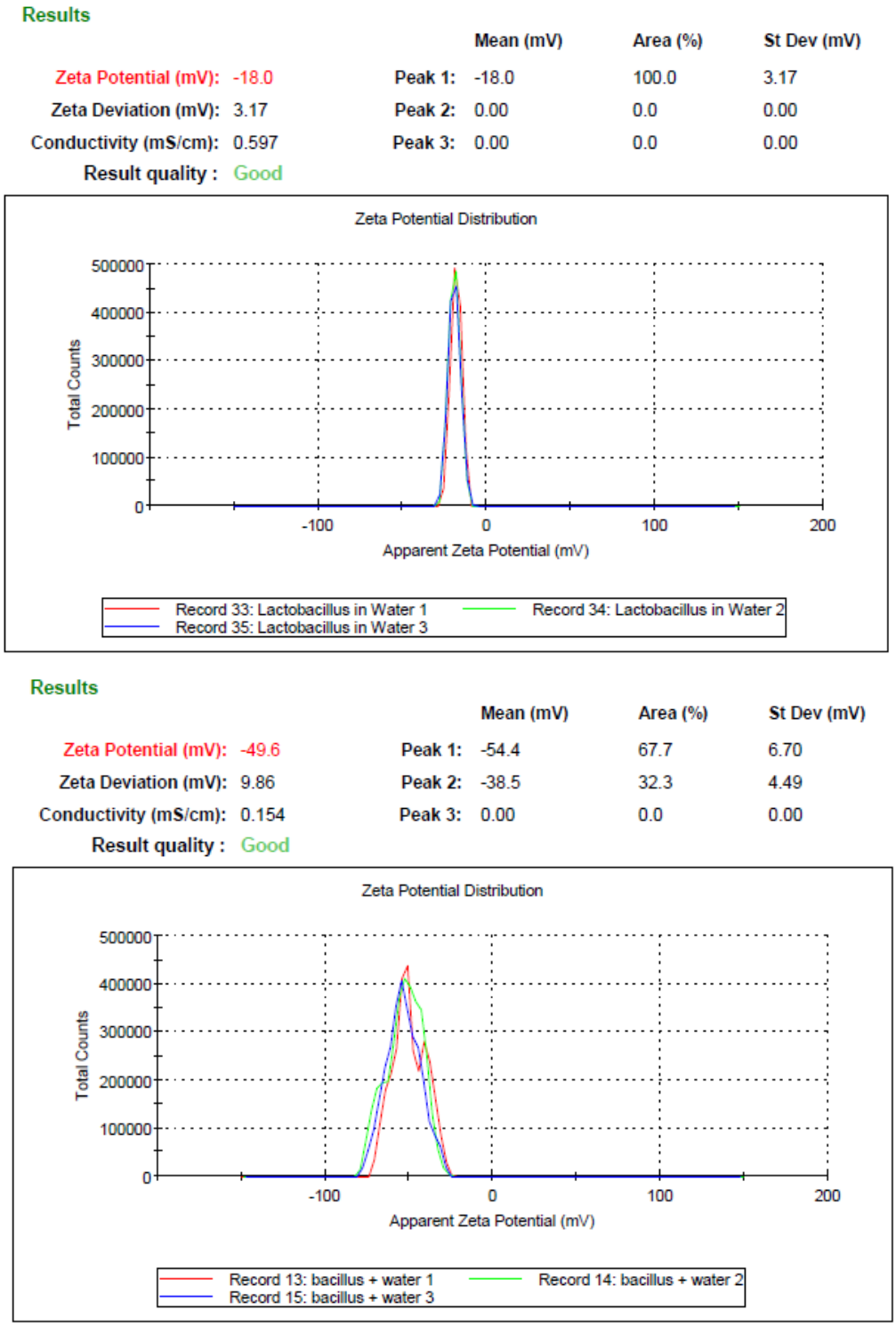

Figure S2. The zeta potential measurements for *L. rhamnosus* in water (top) and *B. subtilis* in water (bottom).

Glycerol Stock Preparation

- *L. rhamnosus* bacteria are grown over 24 hours at 37.0 °C in a shaking incubator
- The optical density is confirmed to be ≥2.0 (OD at 600 nm)
- A 50 vol. % solution of glycerol is prepared by stirring together 10 mL of glycerol with 10 mL DI water until homogeneous
- To a 5 mL glass vial (safe for -80 °C freezing), 2 mL of the 50% glycerol solution is added
- To the same vial, 2 mL of bacterial suspension is added
- The vial is capped and inverted ten times to mix the bacteria and glycerol solution together
- The vial is placed in a -80 °C freezer

Growing Bacteria from Glycerol Stocks

- A flask of MRS broth is prepared for *L. rhamnosus*
- The glycerol stock is removed from the freezer and uncapped
- An autoclaved or other sterile sharp object is used to scrape a small amount of glycerol stock out of the vial
- The scraping is added to the broth, and the flask is gently swirled to help the frozen bacteria disperse
- The vial is recapped and quickly put back in the freezer

Note:

(a) The vial should not remain out long enough to thaw, as this reduces the viability of the bacteria

(b) A properly stored glycerol stock can remain viable for upwards of 10 years, but the more it is handled, the less viable it is. As such, a new stock should be prepared every year or two if it is being handled regularly